

1 **Sequential Data Assimilation for Real-Time Probabilistic**

2 **Flood Inundation Mapping**

3 Keighobad Jafarzadegan*, Peyman Abbaszadeh, Hamid Moradkhani

4 Center for Complex Hydrosystems Research, Department of Civil, Construction, and

5 Environmental Engineering, University of Alabama, Tuscaloosa, AL

6 *Corresponding author: kjafarzadegan@ua.edu

7

8

9

10

11

12

13

14

15

16

17

18

19 **Abstract**

20 Real-time probabilistic flood inundation mapping is crucial for flood risk warning and ~~decision~~
21 ~~decision~~-making during the emergency of an upcoming flood event. Considering the high
22 uncertainties involved in the modeling of a nonlinear and complex flood event, providing a
23 deterministic flood inundation map can be erroneous and misleading for reliable and timely
24 ~~decision~~-~~decision~~-making. The conventional flood hazard maps provided for different return
25 periods cannot also represent the actual dynamics of flooding rivers. Therefore, a real-time
26 modeling framework that forecasts the inundation areas before the onset of an upcoming flood is
27 of paramount importance. Sequential Data Assimilation (DA) techniques are well-known for real-
28 time operation of physical models while accounting for existing uncertainties. In this study, we
29 present a ~~Data Assimilation (DA)~~-hydrodynamic modeling framework where multiple gauge
30 observations are integrated into the LISFLOOD-FP model to improve its performance. This study
31 utilizes the Ensemble Kalman Filter (EnKF) in a multivariate fashion for dual estimation of model
32 state variables and parameters where the correlations among point source observations are taken
33 into account. First, a synthetic experiment is designed to assess the performance of the proposed
34 approach, ~~then~~ the method is used to simulate the Hurricane Harvey flood in 2017. Our results
35 indicate that the multivariate assimilation of point-source observations into hydrodynamic models
36 can improve the accuracy and reliability of probabilistic flood inundation mapping by 5-7%, while
37 it also provides the basis for sequential updating and real-time flood inundation mapping.

38 **Keywords:** Data Assimilation; Probabilistic Flood Inundation Mapping; Hydrodynamic Model;
39 Ensemble Kalman Filter

40

41

42

43

44

45

46 **1. Introduction**

47 The on-time, accurate, and reliable characterization of an upcoming flood event is imperative for
48 proper decision making and risk analysis. A well-calibrated hydrologic model coupled with
49 reliable weather forecast models can be used to generate the streamflow forecast (Clark and Hay,
50 2004; Cuo et al., 2011; Habets et al., 2004). While streamflow forecasting during flood events is
51 indispensable, the critical step for flood risk analysis is to estimate the flood inundation areas
52 corresponding to the forecasted streamflow of a potential upcoming event. Hydrodynamic models
53 are common tools used to simulate the physics of a river system and predict the spatiotemporal
54 distribution of water surface elevation (WSE). The predicted ~~water surface elevation~~ WSE can be
55 simply converted to water depth and inundation area by overlaying with a high-resolution Digital
56 Elevation Model (DEM) (Merwade et al., 2008; Teng et al., 2017). Since floods happen in a short
57 period and at a certain location, it is most-often not possible to find an appropriate remote sensing
58 image that covers those inundated areas during the flood period. This is the main reason that
59 research on flood inundation mapping is mostly limited to post-event analysis where specific study
60 areas with available remote sensing data are used as testbeds.

61
62 ~~According to the literature, most studies have analyzed the flood events for which the flood extent
63 maps were available from surveying or satellite remote sensing. These studies include but are not
64 limited to, calibration and assimilation of hydrodynamic models (Baldassarre et al., 2009; García-
65 Pintado et al., 2013; Gobeyn et al., 2017; Hostache et al., 2009; Lai et al., 2014; Pappenberger et
66 al., 2007; Rahman and Thakur, 2018; Tarpanelli et al., 2013). Depending on the research
67 objectives, such studies are crucial as they address important theoretical questions and advance the~~

68 ~~flood modeling task. For example, several studies have used satellite remote sensing data, such as~~
69 ~~Synthetic Aperture Radar (SAR) images, to find the sensitivity of hydrodynamic models to their~~
70 ~~parameters, compare calibration strategies and test the application of assimilating remote sensing~~
71 ~~data into these models (Di Baldassarre et al., 2009; Hunter et al., 2005; Mason et al., 2009; Matgen~~
72 ~~et al., 2010). Since floods happen in a short period and at a certain location, it is most often not~~
73 ~~possible to find an appropriate remote sensing image that covers those inundated areas during the~~
74 ~~flood period. This is the main reason that research on flood inundation mapping is mostly limited~~
75 ~~to post event analysis where specific study areas with available remote sensing data are used as~~
76 ~~testbeds.~~

77 Federal Emergency Management Agency (FEMA) is the leading agency in the United States that
78 provides flood hazard and risk maps over the Contiguous United States (CONUS). While These
79 these maps display ~~the~~ flood-prone areas corresponding to specific return periods (e.g. 100 and
80 500-year events). ~~While the FEMA flood hazard and risk maps provide general information about~~
81 ~~risk areas~~, they are not always reliable for an upcoming flood event ~~with different return periods~~.

82 For example, FEMA 100-year and 500-year flood hazard maps covered only one-third and half of
83 the inundated areas induced by Hurricane Harvey in Harris County, Texas, respectively (Pinter et
84 al., 2017). The National Water Center Innovators Program proposed the idea of real-time flood
85 inundation mapping across the United States in 2015 (Maidment, 2017). It highlighted the
86 importance of event-based flood inundation mapping where a model uses the forecasted river
87 discharge to estimate the inundation areas corresponding to a specific flood just before the onset
88 of the event. Compared to the traditional flood hazard mapping, real-time flood inundation
89 mapping is more informative and beneficial for emergency response-related decision-making.

90 In real-time flood inundation mapping, the model takes advantage of forecasted forcing data and
91 generates inundation areas corresponding to an upcoming flood event. Providing these maps ahead
92 of time is extremely valuable for building a robust flood warning system. Data assimilation (DA)
93 is an effective approach commonly used to improve the performance of real-time hydrologic
94 forecasting by updating the model state variables and parameters when new observation becomes
95 available (Moradkhani et al., 2019). The integration of DA with physical models is highly
96 advantageous as it enables accounting for different sources of uncertainties involved in model
97 predictions. These include (1) forcing data uncertainty due to the limitation of measurements and
98 spatiotemporal representativeness of the data (Alemohammad et al., 2015; Kumar et al., 2017), (2)
99 parameter uncertainty due to equifinality and non-uniqueness of parameters (Abbaszadeh et al.,
100 2018; Leach et al., 2018), (3) model structural uncertainty due to the imperfect representation and
101 conceptualization of a real system (Abbaszadeh et al., 2019; Pathiraja et al., 2018; Zhang et al.,
102 2019) and (4) initial and boundary condition uncertainty (DeChant and Moradkhani, 2014; Lee et
103 al., 2011).

104 Probabilistic forecasting and uncertainty quantification using DA have been the core of modeling
105 in the atmospheric and oceanic sciences (e.g. Anderson and Anderson, 1999; Courtier et al., 1993).
106 Later, the hydrologic community started to utilize this approach to account for the uncertainties
107 involved in different layers of model predictions and provide a more accurate and reliable model
108 estimates such as estimation of soil moisture (Gavahi et al., 2020; Pauwels et al., 2001; Reichle et
109 al., 2002; Xu et al., 2020), streamflow (Moradkhani et al., 2005a; ~~Vrugt et al., 2006~~), snow
110 (Sheffield et al., 2003; Slater and Clark, 2006) and ~~so many~~ other hydrologic variables. Despite
111 these advances in hydrologic studies, the application of data assimilation in conjunction with
112 hydrodynamic models has received little attention in the literature. The characterization of

113 uncertainty in hydrodynamic models for probabilistic flood inundation mapping has been mostly
114 limited to ~~conventional techniques, such as random~~ Monte Carlo sampling (Ahmadisharaf et al.,
115 2018; Aronica et al., 2012; Domeneghetti et al., 2013; Neal et al., 2013; Papaioannou et al., 2017;
116 Pedrozo-Acuña et al., 2015; Purvis et al., 2008; Savage et al., 2016) and Generalized Likelihood
117 Uncertainty Estimation (GLUE) (Aronica et al., 2002a; Romanowicz and Beven, 2003).

118 The effectiveness and application of assimilating remotely sensed data (e.g. Soil Moisture Active
119 Passive (SMAP)) into hydrologic models have been vastly investigated in the literature
120 (Abbaszadeh et al., 2020; Azimi et al., 2020; Lievens et al., 2017). However, given the small scale
121 of the hydrodynamic modeling process, the spatiotemporal resolution of current satellite products
122 is not adequate for assimilating into these models. ~~To properly estimate the flood inundation~~
123 ~~extent, a spatial resolution less than river width (e.g. 100 m) is recommended. In addition, d~~Due
124 to the short duration of floods, satellite data with ~~daily revisit time~~a sub-daily time scale and spatial
125 resolution less than the river width (e.g. 100 m) is needed~~recommended~~. Since remote sensing
126 products do not provide such high spatiotemporal resolution data for hydrodynamic models, the
127 research on hydrodynamic data assimilation is limited in the literature. ~~Due to the coarse spatial~~
128 ~~resolution of satellites that provide water surface elevation data, s~~Some studies have limited their
129 analyses to large rivers with a width of above 1 km (e.g. study of Nile and Amazon) (Brêda et al.,
130 2019). However, since the width of the majority of rivers is less than 100 meters, these studies
131 cannot be practically used in many regions.

132 -Several studies used higher resolution synthetic Surface Water and Ocean Topography (SWOT)
133 data to evaluate the performance of assimilation techniques (Durand et al., 2008; Munier et al.,
134 2015; Pedinotti et al., 2014; Yoon et al., 2012). While these works provided important information
135 about the assimilation of satellite data into hydrodynamic models, their applications are only

136 limited to synthetic experiments, making them impractical for real case studies. Some studies have
137 implemented indirect methods to estimate WSE from flood extents generated by high-resolution
138 SAR satellite data (Giustarini et al., 2011; Hostache et al., 2010; Matgen et al., 2010b; Neal et al.,
139 2009). This approach can provide high-resolution data that is suitable for the majority of rivers.
140 However, the reliability of this data is concerning because the methods used to convert the flood
141 extent to WSE pose additional errors ~~which that~~ downgrades the quality of the final observed data
142 for assimilation practices. Besides these issues, the major drawback of remote sensing data
143 assimilation pertains to their coarse temporal resolutions. To efficiently monitor the flood
144 dynamics, the assimilation process should be performed at a daily/hourly time scale, however, the
145 revisit frequency of satellites used for capturing the ~~water surface elevation~~WSE ranges from a
146 week to a month. Therefore, there is a significantly low chance to capture multiple real-time remote
147 sensing images for the majority of inundated catchments during flood events. In the most
148 optimistic scenario, assimilation of satellite data is only limited to one/two updates during the
149 simulation period which may not be sufficient for reliable probabilistic flood inundation mapping.

150 Application of DA in hydrodynamic modeling can be either river monitoring or flood inundation
151 mapping. The goal of hydrodynamic data assimilation for river monitoring is to track variations in
152 the channel roughness and bathymetry in the long run. Therefore, the weekly/monthly satellite
153 data can be well assimilated into the models as the channel characteristics do not change on a daily
154 basis. On the other hand, flood inundation mapping needs an hourly/daily track of WSE because
155 floods happen rapidly and affect the river dynamics on a short time scale. The literature indicates
156 those studies that assimilated data into hydrodynamic models have been mostly designed for river
157 monitoring (Brêda et al., 2019; Durand et al., 2008; Yoon et al., 2012b). To capture the daily
158 dynamics of the rivers for real-time flood inundation mapping, the discharge and water stage

159 values measured at the gauge stations can be assimilated into the hydrodynamic models. Xu et al.,
160 (2017) performed a Particle Filtering (PF) approach to assimilate the water stage data from six
161 gauges into a hydrodynamic model. In order to calculate the particle weights in the filtering
162 process, they assumed that gauge observations are independent. In this study, however, we
163 consider interconnections among the gauge stations and apply multivariate Ensemble Kalman
164 Filter (EnKF) to a ~~2D~~-two-dimensional (2D) hydrodynamic model for better characterization and
165 quantification of uncertainty and further improving the accuracy of model simulations.

166 Advancing the probabilistic hydrodynamic modeling with DA techniques is a necessary step to fill
167 the gap between hydrology and hydrodynamics. To address this problem, this study aims to
168 explore the capability of a standard sequential DA technique, namely the EnKF, for real-time
169 probabilistic flood inundation mapping. ~~The p~~Past studies that used the DA in conjunction with
170 hydrodynamic models, have mostly focused on the quantification of uncertainty in one or two
171 hydrodynamic variables ~~;~~ (e.g. Giustarini et al., (2011) and Hostache et al., (2018) only
172 investigated the uncertainty in the upstream flow and rainfall, respectively; Yoon et al., (2012)
173 focused on the uncertainty of river bathymetry while ignoring the roughness parameter
174 uncertainty). In addition, the main application of DA-hydrodynamic modeling framework has been
175 in river monitoring at long-term or water stage forecasting during the flood events (Brêda et al.,
176 2019; Matgen et al., 2010; Xu et al., 2017). However, this study takes one step further and proposes
177 a DA-hydrodynamic modeling framework for real-time probabilistic flood inundation mapping
178 while accounting for ~~all~~-major sources of uncertainties involved in the model simulations including
179 ~~-. These include~~ hydrodynamic model parameters (channel roughness and river bathymetry)
180 ~~uncertainty~~, forcing data (river boundary conditions) ~~uncertainty~~, and state variable (water depth)
181 ~~uncertainty~~. Additionally, unlike past works that assimilated either discharge or water stage into

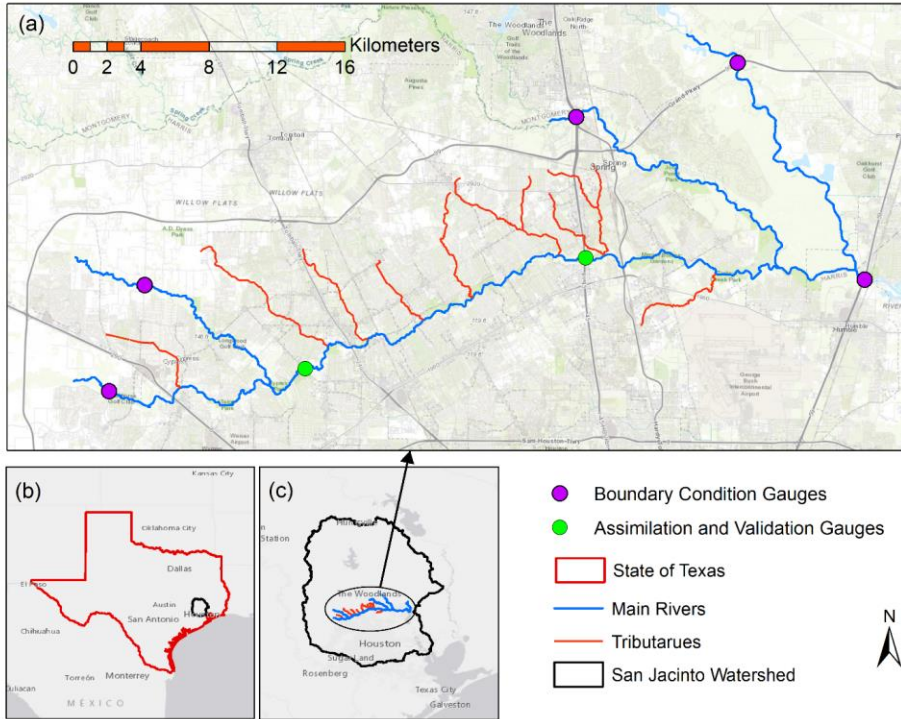
182 the hydrodynamic model, this study performs a multivariate DA to incorporate the observed values
183 of both variables into the hydrodynamic model for a reliable simulation of ~~flooding and its~~
184 ~~corresponding~~-inundation area.

185 **2 Data and Study area**

186 In this study, we simulate the Hurricane Harvey flood, one of the worst natural disasters in the
187 history of the United States that caused more than 120 billion USD ~~in damage~~
188 (https://www.nhc.noaa.gov/data/tcr/AL092017_Harvey.pdf). The Harvey storm hit Texas on
189 August 25, 2017, caused massive precipitation for six continuous days and resulted in extreme
190 flooding condition in Houston and surrounding areas. Given the considerable uncertainties in
191 hydrologic and hydrodynamic processes of such an extreme flood, a deterministic modeling
192 approach with fixed inputs provides erroneous simulations that are highly different from
193 observations. To account for the uncertainties involved in different layers of flood simulation, this
194 study implements a DA-hydrodynamic modeling framework and provides probabilistic flood
195 inundation maps.

196 Figure 1.a shows the study area that consists of four main channels (blue lines) and eight tributaries
197 (red lines). ~~The study area is located in the State of Texas (Figure 1.b) in the middle of the San~~
198 ~~Jacinto watershed (Figure 1.c), a highly developed basin (USGS HUC6 #120401) with the area of~~
199 ~~10400 km². The main channels simulated in the study are around 106 km and draining into three~~
200 ~~HUC8 watersheds: the Spring (#12040102), West Fork San Jacinto (#12040101) and East Fork~~
201 ~~San Jacinto (#12040103). The drainage areas of the channels are relatively flat with an average~~
202 ~~slope of 0.62%, and the soil is mostly impermeable due to the high rate of recent developments in~~
203 ~~this region.~~ The upstream and downstream boundary conditions (purple points) are provided from

204 the daily streamflow in four United States Geological Survey (USGS) gauges ((#08068090, #
205 08068500, #08068740, #08068780) and water stage time series at the downstream gauge
206 (#08069500). The daily streamflow discharge in two internal gauges (green points #08068800 and
207 #08069000) and water stage time series in the second internal gauge are the observations that ~~will~~
208 ~~be~~ assimilated into the LISFLOOD-FP model. Internal gauges refer to those stations located
209 between upstream and downstream of the simulated river system. Figures 1.b and 1.c present the
210 geographic location of the study area within the state of Texas and San Jacinto watershed,
211 respectively. To set up the LISFLOOD-FP model, we use a DEM with 120 m spatial resolution
212 resampled from one arc second (30 m) USGS National Elevation Dataset. Such a coarse resolution
213 DEM alleviates the computational intensity of the proposed probabilistic hydrodynamic modeling
214 framework. It should be noted that the subgrid solver used for simulation of flood has the
215 advantage of accepting narrow rivers with a width of less than 120 m while the cell sizes are 120
216 m. In this study, the DA-hydrodynamic modeling framework is parallelized and performed on the
217 University of Alabama High-Performance Computing (UAHPC) cluster.



218

219 *Figure 1 (a) Study area with all gauges, rivers, and tributaries. (b) Geographic location of San*
 220 *Jacinto Watershed within the state of Texas. (c) Geographic location of the study area within*
 221 *San Jacinto watershed (© NhDplus and USGS).*

222 **3. Methods**

223 **3.1 Flood inundation model**

224 The flood inundation model used in this study is LISFLOOD-FP (Bates and De Roo, 2000), a
 225 raster-based 2D hydrodynamic model that simulates the spatiotemporal distribution of ~~water~~
 226 ~~surface elevation~~ WSE over the study area. The model solves the momentum and continuity
 227 equations (Saint Venont equations):

228
$$\frac{\partial Q}{\partial x} + \frac{\partial A}{\partial t} = 0 \quad (1)$$

229
$$\frac{1}{A} \frac{\partial A}{\partial t} + \frac{1}{A} \frac{\partial(Q^2)}{\partial x} + g \frac{\partial h}{\partial x} - g(S_0 - S_f) = 0 \quad (2)$$

230 where Q is the flow rate at a given cross-section with the area of A in the main channel, x denotes
231 the location along the channel, t represents time, S_0 and S_f are channel bed and friction slopes, and
232 g is the gravitational acceleration.

233 We use the sub-grid channel solver, the most recently developed numerical scheme that considers
234 friction and water slope as well as local acceleration components in the shallow water equations
235 (Neal et al., 2012). This solver is advantageous for large-scale and efficient modeling as it utilizes
236 coarse resolution DEMs along with channel widths ~~values~~ that are smaller than DEM resolution.
237 Since DA-hydrodynamic modeling requires hundreds of model simulations, ~~a computationally~~
238 ~~intensive operation~~, this solver helps reduce the computational burden of each simulation and
239 enables implementing probabilistic flood inundation mapping within a DA framework. To set up
240 the model, we assume rectangular cross-section areas and a uniform roughness for both channel
241 and floodplain. Given the low sensitivity of LISFLOOD-FP to the floodplain roughness (Hall et
242 al., 2005; Horritt and Bates, 2002), this parameter is assumed a constant value. However, the
243 uncertainty of channel roughness is ~~the only model roughness parameter whose associated~~
244 ~~uncertainty is accounted for~~ taken into account within the assimilation framework. We also
245 consider the uncertainty of bathymetry by defining an offset parameter that uniformly lowers the
246 DEM values of the river channels. In addition to model parameters (channel roughness and
247 bathymetry), the upstream and lateral fluxes entered the river system as the boundary conditions
248 of the model are other main sources of uncertainty in the assimilation framework.

249 The upstream boundary conditions are generated from four USGS gauge stations (Figure. 1). To
 250 estimate the lateral fluxes, we calculate the deficit in the system as subtraction of the upstream
 251 from downstream flows and then, distribute the deficit among river tributaries based on their
 252 drainage areas (Please refer to Jafarzadegan et. al (2021) for detailed information about the
 253 calculation of lateral flows in this study area). In section 3.3, we will further discuss the procedure
 254 we used to initialize the model parameters and river boundary conditions.

255 **3.2 Ensemble Kalman Filter (EnKF)**

256 Moradkhani et al. (2005b) provided a comprehensive description of the EnKF formulation for
 257 dual estimation of state and parameters in hydrologic models. Here we briefly describe the EnKF
 258 formulation for multivariate assimilation of point source water stage and discharge data into a
 259 hydrodynamic model. For a more effective assimilation process, both types of interconnections
 260 between observations, namely spatial correlation of a single observation (discharge or water stage)
 261 among different gauges as well as and the correlation between both observations at a single gauge
 262 are taken into account in the EnKF equations. The In this study, EnKF is used to simultaneously
 263 estimate model states and parameters. For this purpose, the parameters should be treated similar
 264 to the state variables with a difference that parameter evolution is generated artificially.

265 Let's assume a DA-hydrodynamic modeling framework with l parameters ($p = 1, 2, \dots, l$), m states
 266 ($s = 1, 2, \dots, m$) and n observations ($j = 1, 2, \dots, n$). The following EnKF equations are described
 267 in accordance with the flowchart shown in Figure 2. In the EnKF, parameter samples can be
 268 generated by adding the noise of η_t with covariance Σ_t^θ to the prescribed parameters.

$$269 \theta_{t+1}^{i-} = \theta_t^{i+} + \tau_t^i \quad \tau_t^i \sim N(0, \eta_{t+1}) \quad \forall \quad \eta_{t+1} = \Sigma_{t+1}^\theta \quad (3)$$

270 Using θ_{t+1}^{i-} and forcing data, a model state ensemble and predictions are generated, respectively.

271 $x_{t+1}^{i-} = f(x_t^{i+}, u_t^i, \theta_{t+1}^{i-}) + \omega_t^i \quad \omega_t^i \sim N(0, Q_t) \quad \forall \quad Q_t = \Sigma_t^x \quad (4)$

272 $\hat{y}_{t+1}^i = h(x_{t+1}^{i-}, \theta_{t+1}^{i-}) + v_{t+1}^i \quad v_{t+1}^i \sim N(0, R_{t+1}) \quad \forall \quad R_{t+1} = \Sigma_{t+1}^y \quad (5)$

273 where x_t , u_t , θ_t and y_t are the vector of the uncertain state variables, forcing data, model
 274 parameters and observation data at time step t , respectively. ω_t represents the model errors due to
 275 the imperfect model, and v_t is the measurement error. Most often, ω_t and v_t are assumed to be
 276 white noises with mean zero and covariance Q_t and R_t , respectively. In addition, the two noises
 277 ω_t and v_t are assumed to be independent.

278 Then we update the parameter ensemble members using the standard Kalman filter equation:

279 $\theta_{t+1}^{i+} = \theta_{t+1}^{i-} + K_{t+1}^\theta (y_{t+1}^i - \hat{y}_{t+1}^i) \quad (6)$

280 where $K_{t+1}^\theta \in \mathbb{R}^{l \times n}$ is the Kalman gain matrix for correcting the parameter trajectories and is
 281 obtained by:

282 $K_{t+1}^\theta = \Sigma_{t+1}^{\theta y} [\Sigma_{t+1}^{yy} + R'_{t+1}]^{-1} \quad (7)$

283 where $\Sigma_{t+1}^{\theta y} \in \mathbb{R}^{l \times n}$ is the cross-covariance matrix of parameter ensemble and prediction ensemble
 284 (Eq. 6). Unlike other studies, and for more realistic characterization of observation and model
 285 errors here the correlation between the errors associated with n observation data are accounted for
 286 during the assimilation process. Therefore, the covariance matrix $R'_t \in \mathbb{R}^{n \times n}$ is a nonzero matrix,
 287 such that the values in the diagonal represent the error associated with each observation data and
 288 all elements lower/upper the main diagonal denote the cross covariance between different
 289 observations (Eq. 7). $\Sigma_t^{yy} \in \mathbb{R}^{n \times n}$ is also a similar covariance matrix with the inclusion of error
 290 correlation between the model simulations (Eq. 8).

$$291 \quad \Sigma_{t+1}^{\theta y}(p, j) = \frac{1}{N} \sum_{i=1}^N [(\theta_{t+1}^{i-}(p) - E[\theta_{t+1}^-(p)])(\hat{y}_{t+1}^i(j) - E[\hat{y}_{t+1}(j)])] \quad (8)$$

$$292 \quad R_{t+1}(j, j') = \begin{cases} R_{t+1} & j = j' \\ \frac{1}{N} \sum_{i=1}^N [(y_{t+1}^i(j) - E[y_{t+1}(j)])(y_{t+1}^i(j') - E[y_{t+1}(j')])] & j \neq j' \end{cases} \quad (9)$$

$$293 \quad \Sigma_{t+1}^{yy}(j, j') = \frac{1}{N} \sum_{i=1}^N [(\hat{y}_{t+1}^i(j) - E[\hat{y}_{t+1}(j)])(\hat{y}_{t+1}^i(j') - E[\hat{y}_{t+1}(j')])] \quad (10)$$

$$294 \quad E[\theta_{t+1}^-] = \frac{1}{N} \sum_{i=1}^N \theta_{t+1}^{i-} \quad (11)$$

$$295 \quad E[\hat{y}_{t+1}] = \frac{1}{N} \sum_{i=1}^N \hat{y}_{t+1}^i \quad (12)$$

296 Now using the updated parameter, the new model state trajectories (state forecasts) and prediction
297 trajectories are generated:

$$298 \quad x_{t+1}^{i-} = f(x_{t+1}^{i+}, u_t^i, \theta_{t+1}^{i+}) + \omega_t^i \quad \omega_t^i \sim N(0, \Sigma_t^x) \quad \forall \quad Q_t = \Sigma_{t+1}^x \quad (13)$$

$$299 \quad \hat{y}_{t+1}^i = h(x_{t+1}^{i-}, \theta_{t+1}^{i+}) + v_{t+1}^i \quad v_{t+1}^i \sim N(0, \Sigma_{t+1}^y) \quad \forall \quad R_{t+1} = \Sigma_{t+1}^y \quad (14)$$

300 Model states ensemble is similarly updated as follows:

$$301 \quad x_{t+1}^{i+} = x_{t+1}^{i-} + K_{t+1}^x (y_{t+1}^i - \hat{y}_{t+1}^i) \quad (15)$$

$$302 \quad y_{t+1}^i = y_{t+1}^i + v_{t+1}^i \quad v_{t+1}^i \sim N(0, R_{t+1}) \quad \forall \quad R_{t+1} = \Sigma_{t+1}^y \quad (16)$$

303 where $K_{t+1}^x \in \mathbb{R}^{m \times n}$ is the Kalman gain for correcting the state trajectories and is obtained by:

$$304 \quad K_{t+1}^x = \Sigma_{t+1}^{xy} [\Sigma_{t+1}^{yy} + R_{t+1}]^{-1} \quad (17)$$

305 where $\Sigma_{t+1}^{xy} \in \mathbb{R}^{m \times n}$ is the cross-covariance matrix of states ensemble and prediction ensemble
306 (Eq. 16).

$$307 \quad \Sigma_{t+1}^{xy}(s, j) = \frac{1}{N} \sum_{i=1}^N [(x_{t+1}^{i-}(s) - E[x_{t+1}^-(s)])(\hat{y}_{t+1}^i(j) - E[\hat{y}_{t+1}(j)])] \quad (18)$$

308 $E[x_{t+1}^-] = \frac{1}{N} \sum_{i=1}^N x_{t+1}^{i-}$ (19)

309 In this study the water depth along the channel is the only state variable ($m=1$). The channel
310 roughness and bathymetry are two model parameters ($l=2$) and three point source observations
311 including water discharge at gauge 1 and 2 as well as water stage at gauge 2 ($n=3$) are assimilated
312 into the LISFLOOD-FP model (Table 1). Therefore, the Kalman gains used to update the model
313 parameters and states (Eqs 5 and 15) are 2×3 and 1×3 matrices that take advantage of a
314 multivariate point source assimilation while considering the downstream correlation between
315 discharge observations and the correlation between water stage and discharge at gauge 2.

316 **3.3. Experimental design DA-hydrodynamic modeling framework**

317 ~~The ultimate goal of this study is to simulate the Hurricane Harvey flood and generate probabilistic~~
318 ~~flood inundation maps through the DA hydrodynamic modeling framework.~~ Figure. 1 illustrates
319 the flowchart of the proposed DA-hydrodynamic modeling framework used for real-time
320 probabilistic flood inundation mapping approach. In this study, the EnKF is performed based on
321 an ensemble size of 100. The boundary conditions including four upstream flows, seven lateral
322 fluxes, and downstream flows are perturbed with adding white noises sampled from a normal
323 distribution with a mean zero and relative error of 20%. The errors are assumed heteroscedastic
324 meaning that their values are proportional to the flow magnitude. (Pelletier, (1988) conducted a
325 literature review on the uncertainty of recorded flow at rivers and demonstrated that the error varies
326 in the range 8%-20%. Later, Di Baldassarre and Montanari, (2009) found that the uncertainty of
327 extreme flows can exceed to 25% due to the extrapolating the rating curves. -To characterize
328 uncertainty in the initial condition, namely water depth, we add a white noise with a mean zero
329 and standard deviation of 1 meter. In this study, using the proposed EnKF-based multivariate

Formatted: Font: Italic, Complex Script Font: Italic

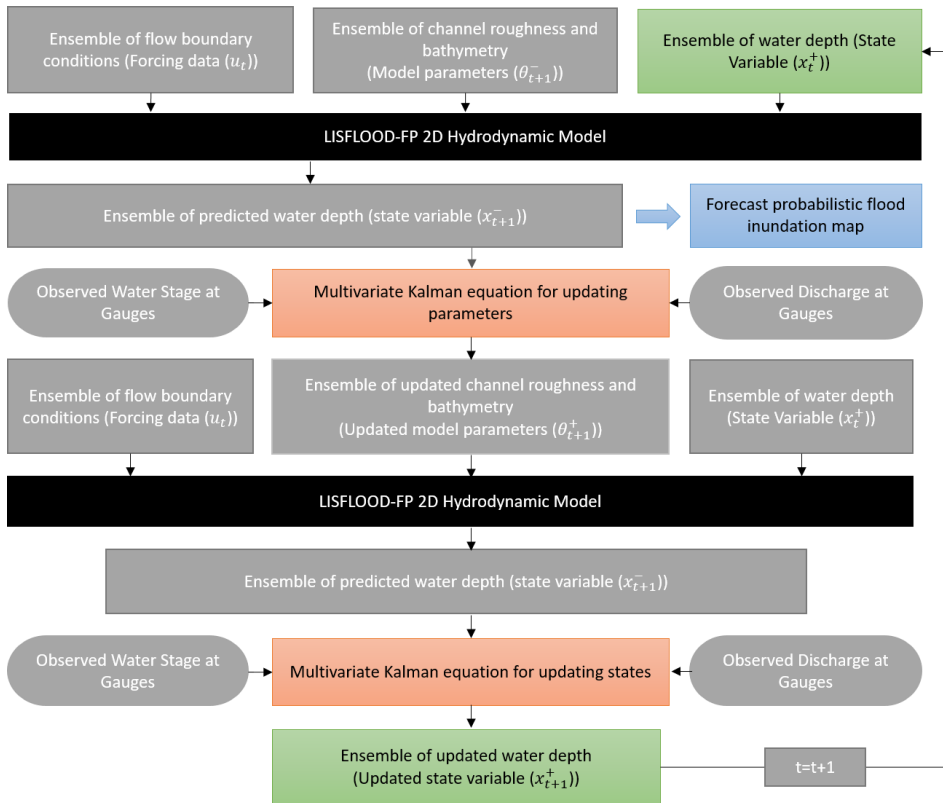
330 assimilation approach, three point-scale observations, i.e., discharge at USGS gauges 1 and 2, as
331 well as water stage at gauge 2, are incorporated into the LISFLOOD-FP model to rectify its state
332 variables and parameters, and hence provide more accurate and reliable flood inundation maps.

333 ~~All these three observations are perturbed by adding a normally distributed white noise with a~~
334 ~~mean zero and a relative error of 20%.~~ First, the LISFLOOD-FP model is forced with the
335 upstream, downstream and lateral flow ensembles. To initialize the state variables in the system,
336 the simulated water depth values at the ending day of the warm-up period (the initial condition for
337 the first day of the model simulation) are perturbed with adding a white noise with a mean zero
338 and standard deviation of 1 meter. It is worth mentioning that the error terms used for the observed
339 flows and the initial water depth are determined through a manual tuning to achieve the most
340 reliable predictions during the simulation. The model parameters (i.e., channel roughness and
341 bathymetry) are initialized using the Latin Hypercube Sampling method and evolved during the
342 assimilation process. The ensemble of water depth values predicted by the model for the next time
343 step together with observations, namely water stage and discharge at gauges are used in the
344 multivariate Kalman equation to update the model parameters. The LISFLOOD-FP model is run
345 for the second time with the updated parameters and the second multivariate Kalman equation uses
346 the predicted water depth with observations to update the ensemble of water depth in the system.

347 The ensemble of updated water depth (state), bathymetry, and channel roughness (parameters) ~~will~~
348 ~~be~~ used within the LISFLOOD-FP to predict an ensemble of water depth for the next time step.
349 The predicted water depth is simply converted to a probabilistic flood inundation map. Using this
350 data assimilation framework, we can generate 1-day forecast of probabilistic flood inundation
351 maps which would be highly beneficial for real-time flood warning and decision making. ~~It is~~
352 ~~worth mentioning that the forecasted probabilistic maps account for different sources of~~

353 ~~uncertainty including the forcing data (boundary condition flows), model parameters (channel~~
354 ~~roughness and bathymetry), and initial conditions (water depth).~~

355 The simulation period of the LISFLOOD-FP model is set up for 45 days from July-30-2017 to
356 Sep-12-2017 and the entire month of July is used as a warm-up period. The model time step and
357 the Courant number are set to 1 second and 0.7, respectively, and the model is simulated at daily
358 scale. The water depth generated for the end of July ~~will be~~ used as the initial condition of the
359 model. To account for the uncertainty of channel roughness and bathymetry, we sample ~~them~~ these
360 variables from uniform distributions ranging from [0, 0.1] and [39, 42] m, respectively. The
361 bathymetry parameter is the elevation of the channel bed at the upper location of the channel. The
362 offset parameter is calculated by subtracting this value from DEM at the upper location. Then, the
363 bathymetry vector that includes the channel bed elevation for all channel cells is generated by
364 subtracting the offset from DEM values along the channel. It should be noted that the range of
365 uniform distribution for channel roughness is chosen based on previous studies (Aronica et al.,
366 2002b; Bales and Wagner, 2009; Di Baldassarre et al., 2009; Horritt, 2006; Pappenberger et al.,
367 2008) while the error range assumed for the bathymetry is mostly determined based on ~~expert~~
368 judgment, and trial-and-error. Since the real magnitude and distribution of these errors have not
369 been fully understood in the literature, their estimated values may not be ~~necessarily the physically~~
370 correct terms and their estimation is ill-posed according to Renard et al., (2010).



371

372 *Figure 2. Schematic of the DA-hydrodynamic modeling framework for real-time probabilistic*
 373 *flood inundation mapping. The green boxes represent the state variables where their updated*
 374 *values are fed into the LISFLOOD-FP model and provide a probabilistic flood inundation map*
 375 *at the forecast mode (blue box). The black boxes highlight the physical model and the orange*
 376 *boxes represent the Kalman equations used for updating the parameter and state variables by*
 377 *the EnKF.*

378 **3.4 Experimental Design**

379 To assess the effectiveness and robustness of the proposed assimilation framework for
 380 probabilistic flood inundation mapping, we design ~~three two different~~ experiments. ~~First, an open-~~
 381 ~~loop (OL) simulation is established where the model is run without assimilation.~~ In the ~~second first~~
 382 experiment, we perform DA-hydrodynamic modeling on a synthetic case study where we assume

Formatted: Normal, Line spacing: single

Formatted: Font: (Default) +Headings CS (Times New Roman), 14 pt, Bold, Complex Script Font: +Headings CS (Times New Roman), 14 pt, Bold

Formatted: Font: 14 pt, Bold, Complex Script Font: 14 pt, Bold, Check spelling and grammar

383 the model is perfect and has no error. In this approach, we set the model parameters (channel
384 roughness and bathymetry), initial state (water depth) and boundary condition flows to fixed values
385 and run the model to generate discharge and ~~water surface elevation~~WSE across the gauges within
386 the study area. These predicted values are assumed as benchmark observations. This synthetic
387 analysis ensures that the assimilation process performs well and the model parameters end up
388 converging to predefined values. In the ~~next step~~second experiment, we implement the proposed
389 assimilation framework on a real case study where the observed discharge and ~~water surface~~
390 ~~elevation~~WSE data that are recorded from the USGS gauges during Hurricane Harvey, are
391 assimilated into the model. In both experiments, we implement an open-loop (OL) simulation
392 where the model is run without an assimilation. The WSE and flood extent maps generated by OL
393 are compared with the results provided by the EnKF in the synthetic and real case studies.
394 Considering the severe flood condition during the Hurricane, we aim to investigate the extent to
395 which the multivariate DA-Hydrodynamic modeling framework improves the model simulation
396 and flood inundation mapping skill.

397 **3.4.5 Validation strategy**

398 As mentioned before, the convergence of uncertain model parameters toward truth in the
399 synthetic experiment demonstrates the performance of DA-hydrodynamic modeling framework.
400 To provide a robust analysis of each assimilation run, it is necessary to assess the model
401 performance through multiple deterministic (*KGE* and *RMSE*) and probabilistic (*NRR* and
402 *Reliability*) measures. The summary of The four performance measures used in this study, namely
403 Kling Gupta Efficiency (*KGE*), Root Mean Square Error (*RMSE*), Normalized Root Mean Square
404 Error Ratio (*NRR*) and *Reliability* is tabulated in Table 4 are calculated using Eqs. 20-23,
405 respectively.

Formatted: Font: Italic, Complex Script Font: Italic

406

407

408 **Table 1: Summary of performance measures used in this study**

| Performance Measure | Mathematical Representation |
|--|---|
| Kling-Gupta Efficiency (KGE) | $1 - \sqrt{\left(\left(\frac{\text{Cov}_{y_t y'_t}}{\sigma \sigma'}\right) - 1\right)^2 + \left(\left(\frac{\sigma'}{\sigma}\right) - 1\right)^2 + \left(\left(\frac{\mu'}{\mu}\right) - 1\right)^2}$ |
| Root Mean Square Error (RMSE) | $\sqrt{\frac{1}{T} \sum_{t=1}^T (y'_t - y_t)^2}$ |
| Normalized Root-Mean-Square Error Ratio (NRR) | $\sqrt{\frac{1}{T} \sum_{t=1}^T (y_t - \bar{y}'_{\bullet,t})^2} \times \left(\frac{1}{T} \sum_{t=1}^T \sqrt{\frac{1}{T} \sum_{t=1}^T (y_t - \bar{y}'_{\bullet,t})^2} \right)^{-1} \sqrt{\frac{N+1}{2N}}$ |
| Reliability | $1 - \frac{2}{T} \sum_{t=1}^T \left \frac{Z_t}{T} - U_t \right $ |

409

410
$$1 - \sqrt{\left(\left(\frac{\text{Cov}_{y_t y'_t}}{\sigma \sigma'}\right) - 1\right)^2 + \left(\left(\frac{\sigma'}{\sigma}\right) - 1\right)^2 + \left(\left(\frac{\mu'}{\mu}\right) - 1\right)^2} \quad (20)$$

411
$$\sqrt{\frac{1}{T} \sum_{t=1}^T (y'_t - y_t)^2} \quad (21)$$

412
$$\sqrt{\frac{1}{T} \sum_{t=1}^T (y_t - \bar{y}'_{\bullet,t})^2} \times \left(\frac{1}{T} \sum_{t=1}^T \sqrt{\frac{1}{T} \sum_{t=1}^T (y_t - \bar{y}'_{\bullet,t})^2} \right)^{-1} \sqrt{\frac{N+1}{2N}} \quad (22)$$

413
$$1 - \frac{2}{T} \sum_{t=1}^T \left| \frac{Z_t}{T} - U_t \right| \quad (23)$$

Formatted: Indent: First line: 0"

Formatted: Font: (Default) +Headings CS (Times New Roman), 12 pt, Complex Script Font: +Headings CS (Times New Roman), 12 pt

Formatted: Font: (Default) +Headings CS (Times New Roman), 12 pt, Complex Script Font: +Headings CS (Times New Roman), 12 pt

414 ~~where~~ y_t and y'_t are the observed and simulated values, respectively. The Kling–Gupta Efficiency
415 (~~*KGE*~~) varies from $-\infty$ to 1, such that a value of 1 indicates a perfect fit between observed and
416 simulated values. The pairs of (μ, σ) and (μ', σ') represent the first two statistical moments
417 (means and standard deviations) of y_t and y'_t , respectively. ~~Root-mean-squared-error (*RMSE*)~~ is
418 the square root of the mean of the square of all of the errors between the predicted and observed
419 values.

Formatted: Font: Italic, Complex Script Font: Italic

Formatted: Font: Italic, Complex Script Font: Italic

420 ~~*NRR*~~ (DeChant and Moradkhani, 2012) is calculated to measure the ensemble spread and assess
421 how confidently the ensemble mean is statistically distinguishable from the ensemble spread.
422 ~~*Reliability*~~ (Renard et al., 2010b) is a measure of the fit of the Q-Q quantile plot to a uniform. A
423 value of 1 is exactly uniform and a value of 0 is the farthest possibility from uniform. For the
424 description of the z_t and U_t calculation, we refer the readers to Renard et al. (2010b).

Formatted: Font: Italic, Complex Script Font: Italic

Formatted: Font: Italic, Complex Script Font: Italic

425 The above four performance measures assess the dynamic behavior of DA-hydrodynamic
426 modeling framework at two specific points. Moreover, to spatially evaluate the behavior of the
427 proposed framework, we compare the maximum probabilistic flood inundation maps (union of
428 probabilistic maps over the simulation period) with the observed floodplain map delineated
429 aftermath of Harvey. The Receiver Operating Characteristic (ROC) graph is a common tool for
430 validating probabilistic classifiers (Fawcett, 2006). Consider a deterministic flood map as a binary
431 map where one and zero represent flooded and non-flooded cells, respectively. First, a threshold
432 in the range of [0,1] is used to convert the probabilistic map to a binary deterministic map. This
433 means all cells with the probability of inundation less than a given threshold are converted to zero
434 and other cells are set to one. The binary map is compared with the reference map and the rate of
435 true positive (~~*rtp*~~) and false positive (~~*rfp*~~) are calculated using Equations ~~7-24~~ and ~~8-25~~
436 (Jafarzadegan and Merwade, 2017):

Formatted: Font: Italic, Complex Script Font: Italic

Formatted: Font: Italic, Complex Script Font: Italic

$$437 \quad rtp = \frac{\text{True positive instances}}{\text{total positives}} \quad (724)$$

$$438 \quad rfp = \frac{\text{False positive instances}}{\text{total negative}} \quad (825)$$

439 where true and false positive instances represent the total number of flooded cells in the reference
 440 map that are predicted as flood and non-flooded cells, respectively. Total positives and negatives
 441 are total flooded and non-flooded cells in the reference map. This process is repeated and a set of
 442 points (rfp, rtp) are generated corresponding to different thresholds. The ROC graph connects the
 443 points in the rfp - rtp space and the area under the curve (AUC) represents the performance of the
 444 probabilistic classifier (Fawcett, 2006). In this study, we use AUC to compare the performance of
 445 OL simulation with the EnKF for probabilistic flood inundation mapping. The Fit (F) index is
 446 another performance measure widely used to compare two deterministic flood extent maps in the
 447 literature (Alfieri et al., 2014; Bates and De Roo, 2000; Sangwan and Merwade, 2015; Tayefi et
 448 al., 2007).

$$449 \quad F = \frac{\text{True positive instances}}{\text{Total positives} + \text{False positives}} \times 100 \quad (26)$$

450 -In addition, we calculate the Underprediction and Overprediction Flood Indices (UFI and OFI)
 451 introduced by Jafarzadegan et al., (2018) for comparing probabilistic flood maps against
 452 deterministic reference maps:

$$453 \quad UFI = \frac{\sum_{i=1}^N (1 - P_i)}{N} \times 100 \quad i \in FI \quad (927)$$

$$454 \quad OFI = \frac{\sum_{j=1}^M (P_j)}{M} \times 100 \quad j \in NFI \quad (1028)$$

455 where FI and NFI denote the flooded and non-flooded regions in the reference map, and i and j are
 456 indicators of cells located within these regions. N and M are the total number of cells in the FI and

Formatted: Font: Italic, Complex Script Font: Italic

457 NFI regions and P_i, P_j denote the probability of inundation for cells i and j derived from the
458 probabilistic flood maps.

Formatted: Font: Italic, Complex Script Font: Italic

Formatted: Font: Italic, Complex Script Font: Italic

Formatted: Font: Italic, Complex Script Font: Italic

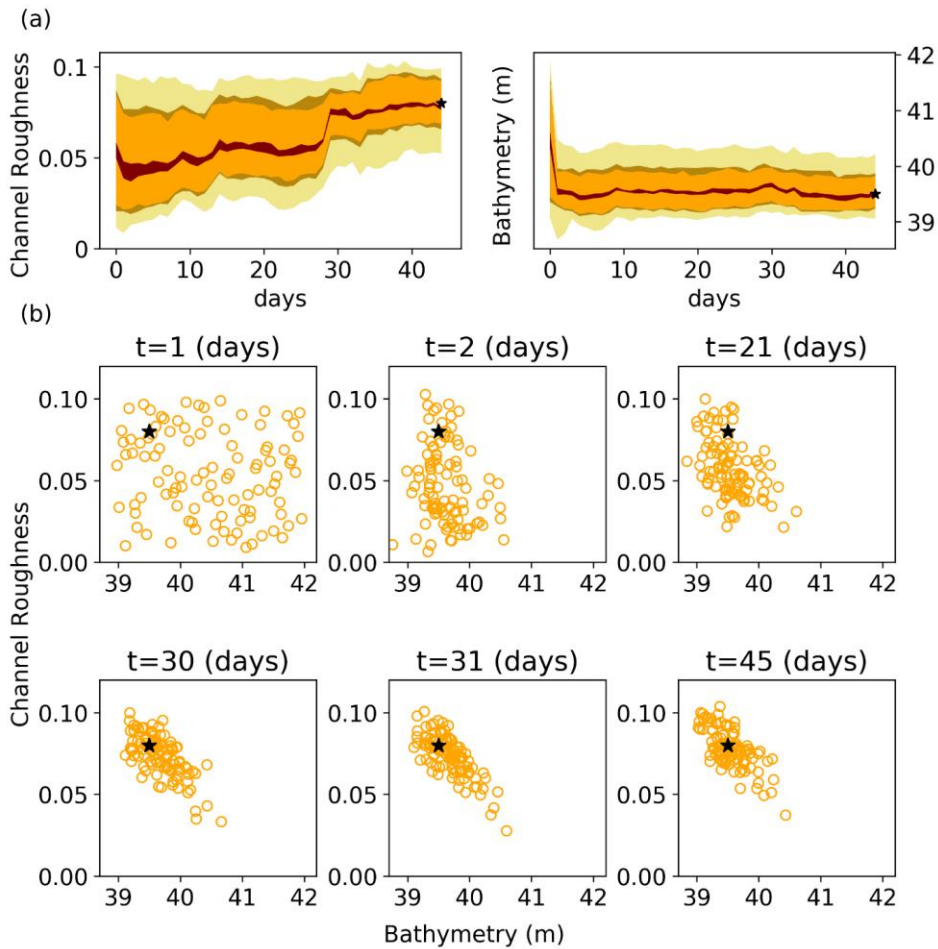
459 4. Results

460 4.1 Experiment 1: Synthetic Case Study

461 We conduct the synthetic experiment to ensure the usefulness and effectiveness of the proposed
462 DA-hydrodynamic modeling framework. Figure 3.a presents uncertainty bound evolution of the
463 parameters in the LISFLOOD-FP model (i.e., channel roughness and bathymetry) for 45 days
464 assimilation of synthetic observations (i.e., discharge at gauges 1 and 2 and water stage at gauge
465 2). ~~The shaded areas correspond to 95, 75, 68, and 10 percentile predictive intervals, and the black~~
466 ~~stars at the end of each parameter subplot represent the true parameter values.~~ It is worth
467 mentioning that the uncertainty of bathymetry shown in this Figure corresponds to the channel bed
468 elevation at the upper location of the channel. As seen both parameters converge smoothly to the
469 certain region in parameter space where the uncertainty bounds stabilize. While the uncertainty
470 bound associated with the bathymetry becomes stabilized at the early stage of the assimilation
471 process, for the channel roughness, the uncertainty bound ~~gets-is~~ stabilized toward the end of the
472 assimilation period. It is also evident from Figure 3.a that the bathymetry is a more identifiable
473 parameter compared to the channel roughness as it shows the fastest convergence with a minimum
474 degree of uncertainty. However, the channel roughness is less identifiable with the slowest
475 convergence. ~~The scatter plots illustrate the evolution of parameter space at six different time~~
476 ~~segments.~~ In Figure 3.b, ~~The~~ the first day ($t=1$) includes all 100 ensemble members of parameters
477 and day 30 corresponds to the highest discharge and water stage of flooding when the model
478 parameters reach the highest improvement and get closer to the true value. Figure 3.b shows that

Formatted: Font: Italic, Complex Script Font: Italic

479 both model parameters are converging toward the true values as the assimilation proceeds. This
 480 indicates the efficacy and usefulness of the proposed DA-hydrodynamic modeling framework
 481 developed in this study.



482
 483 *Figure 3. Temporal evolution of the LISFLOOD parameters for the synthetic experiment during*
 484 *Hurricane Harvey using the EnKF. (a) Temporal evolution of model parameter predictive*
 485 *intervals (shaded areas) corresponding to 95, 75, 68, and 10 percentile (b) Temporal evolution*

486 of particle positions in the model parameter space at six different days during the Hurricane.
487 The shaded areas correspond to 95, 75, 68, and 10 percentile predictive intervals, and the
488 black stars at the end of each parameter subplot represent the true parameter values.

489

490

491 **4.2 Experiment 2: Real Case Study**

492 In the real experiment, we assimilate the discharge and water stage readings from two ~~internal~~
493 USGS gauges into the LISFLOOD-FP model. We also run the OL simulation and calculate the
494 ensemble mean to predict the discharge and water stage at these two gauges. Figure 4 presents a
495 comparison of simulated discharge (Figures 4a ~~and~~, 4b) and water stage (Figures 4c ~~and~~, 4d) with
496 observations using both OL and our EnKF-based approach. Figures 4a and 4c are the prior
497 estimates of discharge and water stage, while Figures 4b and 4d show their posterior ~~distributions~~
498 ~~which that~~ reflect the updated variables after assimilating the observations into the model. It is
499 worth mentioning that although prior ~~distributions~~ represent the results before assimilating new
500 observations into the model, their values are dependent on the initial conditions updated from
501 observations in the previous time step. ~~In this study, s~~Since forecasting (1-day lead time) is the
502 main objective of DA-hydrodynamic modeling framework, we specifically focus on behavior of
503 priors. As can be seen, the simulated peak discharge by the OL is highly overestimated by around
504 200 ~~ems-m³/s~~ while assimilating the observations improve the results so that their difference with
505 observation is less than 50 ~~m³/s ems~~ at the peak of the flood ($KGE = 0.76$ and $RMSE = 40.9$
506 ~~m³/s ems~~). In contrast, the simulated water stage in Figures 4c and 4d are underestimated by OL
507 by around 2 meters at the peak. Compared to the OL, Using using the developed EnKF approach
508 raises the peak of water stage at peak and reduces the errors significantly ($KGE = 0.96$ and
509 $RMSE = 0.5$ m). The accurate estimates of prior discharge and water stage confirm the applicability

Formatted: Superscript

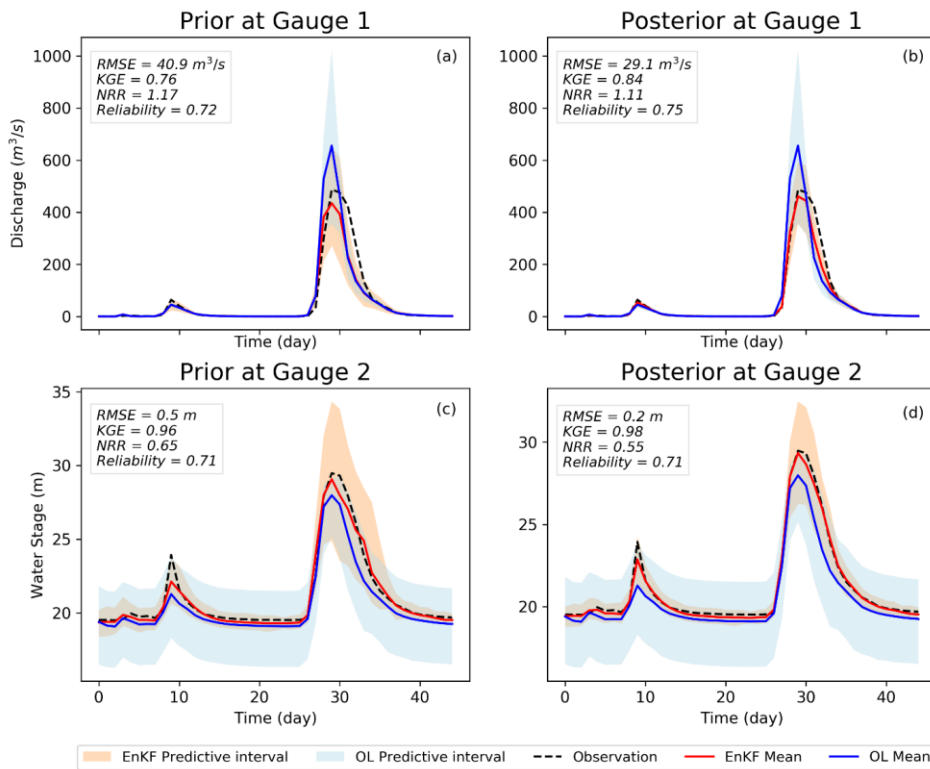
Formatted: Font: Italic, Complex Script Font: Italic

510 of the proposed assimilation framework in forecast mode when real-time flood warning and
 511 decision making is the priority. The NRR measure for the prior discharge and water stage are 1.17
 512 and 0.65, showing that the uncertainty bound is underestimated and overestimated, respectively.
 513 The ~~reliability~~ Reliability of both variables is above 70 percent since the uncertainty bounds
 514 encompass the observations for almost the entire simulation period.

Formatted: Font: Italic, Complex Script Font: Italic

Formatted: Font: Italic, Complex Script Font: Italic

515

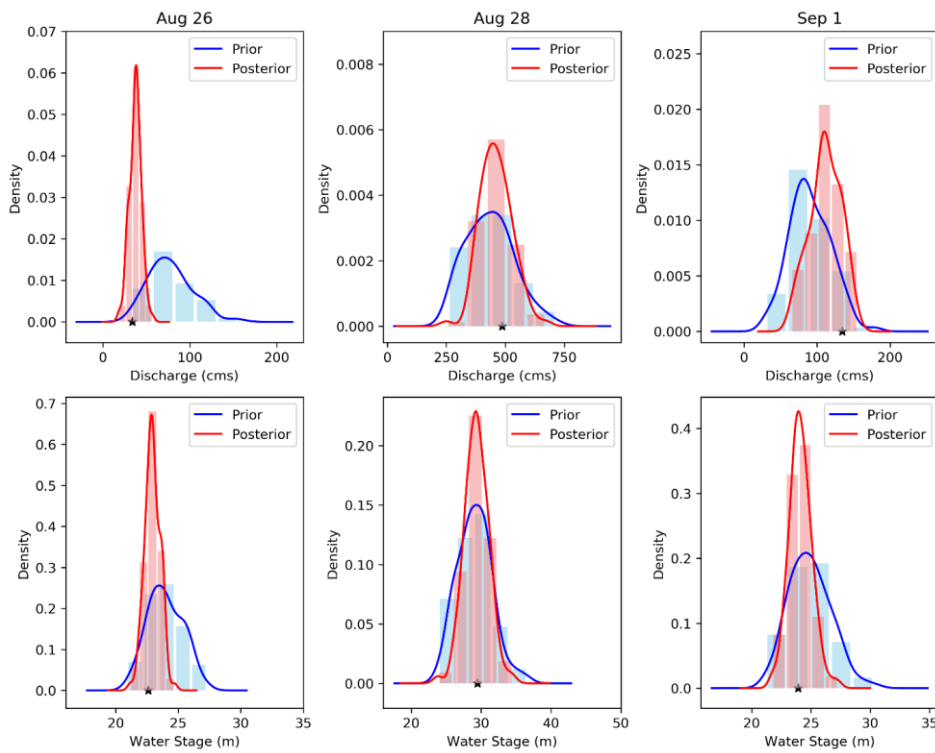


516

517 *Figure 4 Simulation results of LISFLOOD-FP for the real experiment during Hurricane Harvey*
 518 *using the EnKF and open-loop. (a) Prior simulated discharge at gauge 1 (b) Posterior simulated*
 519 *discharge at gauge 1 (c) Prior simulated water stage at gauge 2 (d) Posterior simulated water*

520 *stage at gauge 2. The shaded areas represent the predictive interval of simulated discharge and*
521 *water stage by EnKF.*

522 Figure 5 illustrates the prior and posterior distributions of discharge and water stage in the
523 beginning, peak, and ending days of Hurricane Harvey flood. In all three days, the uncertainty
524 bounds of both discharge and water stage are narrowed down by assimilating the observations so
525 that posterior distributions are more precise compared to the priors. In the beginning and ending
526 days (Aug 26 and Sep 1), the mean of prior distributions is substantially shifted toward truth in the
527 posterior distributions. Figure 5 reveals that our developed approach provides more accurate and
528 reliable posterior discharge and water stage distributions compared to prior distributions where the
529 simulations are either overestimated or underestimated. It is noted that, on August 28 (day of flood
530 peak), although the prior distributions accurately represent the observation, they have a wide
531 uncertainty bound. After correcting/updating the model state variables and parameters, as posterior
532 distributions show, the uncertainty bound is reduced while the ensemble mean remains closer to
533 the observation.



534

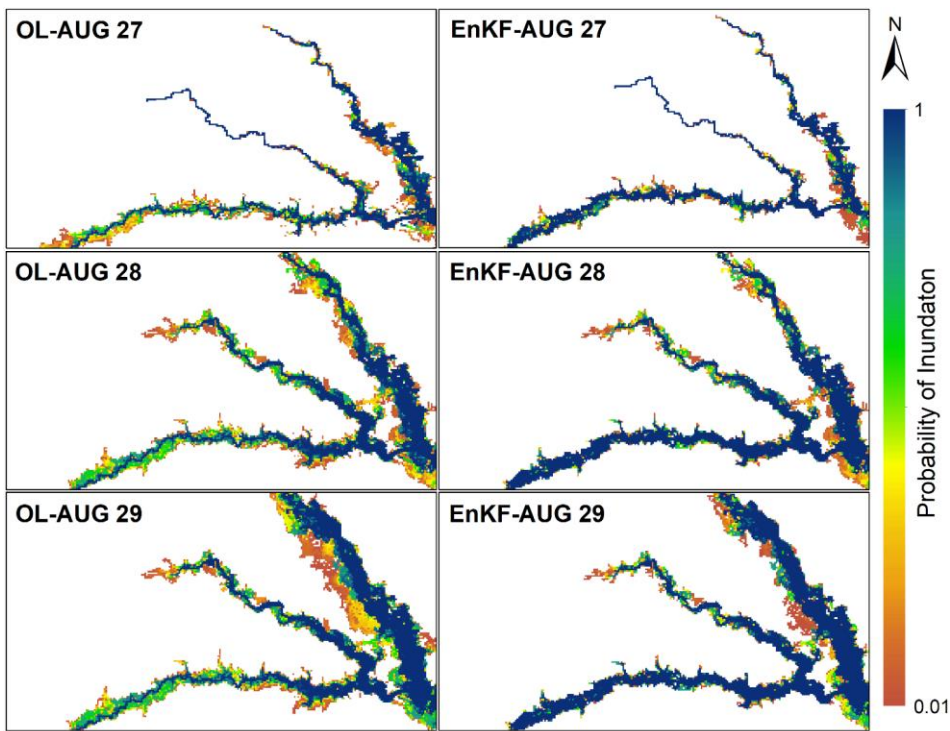
535 *Figure 5. Prior and posterior distribution of discharge (a,b,c) and water stage (c,d,f) at the*
 536 *beginning (Aug 26), peak (Aug 28), and ending (Sep1) days of Hurricane Harvey using the*
 537 *EnKF*

538

539 **4.3 Probabilistic Flood Inundation Mapping**

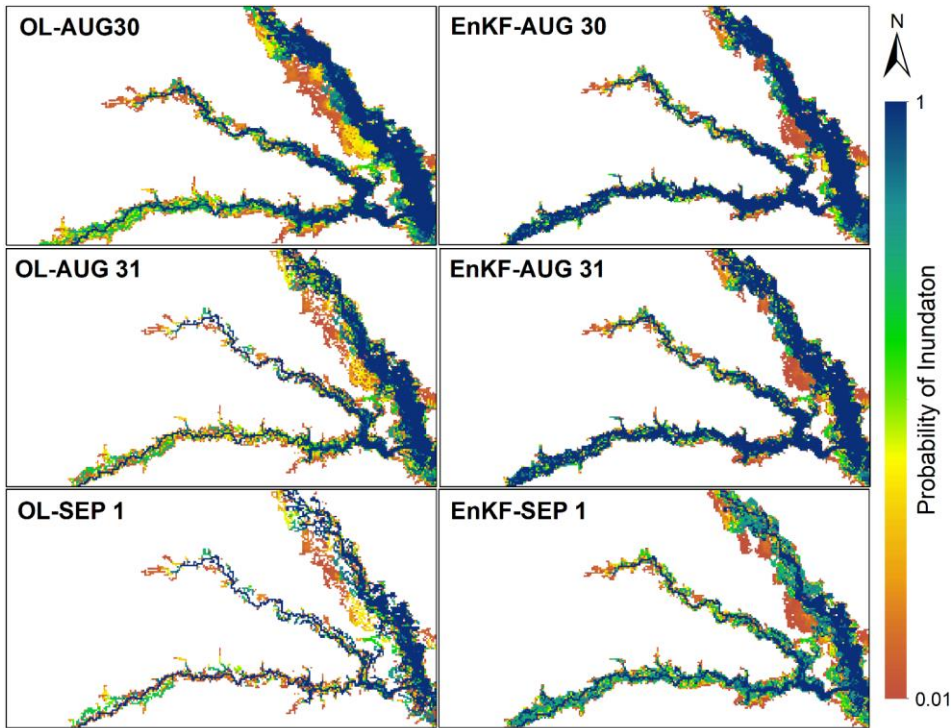
540 In this ~~studysection~~, we ~~propose a DA hydrodynamic modeling framework to~~ account for the
 541 uncertainties involved in flood modeling and generate real-time probabilistic flood inundation
 542 maps. Since the majority of flooding conditions occurred within ~~6-six~~ days from August 27-Sep 1,
 543 we display the spatial distribution of water depth in this period and provide probabilistic flood

544 inundation maps using both OL and our developed approach (see Figures 6 and 7). Figure 6
545 represents the first three days of Harvey, which corresponds to the upper limb of the flood
546 hydrograph. On August 27, the major difference between the OL and EnKF appears in the regions
547 around the upstream of the lower channel where the EnKF provides a more reliable prediction of
548 the inundated area. Moving toward the peak of flood on Aug 29, the OL generates a large region
549 of uncertain cells around the banks of the upper channel, while both the extent and density of
550 uncertain values in the probabilistic maps generated by the EnKF is smaller during the peak of
551 Harvey.



553 *Figure 6 Probabilistic flood inundation maps generated by OL and EnKF techniques to simulate*
554 *the upper limb of Harvey flood hydrograph from Aug 27 to Aug 29.*

555 Figure 7 shows the probabilistic inundation areas in the last three days corresponding to the lower
556 limb of the flood hydrograph. ~~In this figure, t~~The discrepancies between the OL and EnKF flood
557 maps increase showing that performing DA is more effective in improving the inundation mapping
558 skill from peak to ending point of the flood hydrograph. A large number of inundated cells
559 generated by the OL are vanished after the peak of Harvey which results in a set of scattered
560 discontinuous maps in Aug 31 and Sep 1. On the other hand, the probabilistic maps generated by
561 the EnKF maintain their continuous shapes so that the probability of inundation is reduced without
562 changing the extent. The merit of the EnKF in improving the flood inundation areas at the lower
563 limb of the flood hydrograph agrees with results in Figures 4c and 4d where the EnKF widens the
564 simulated water stage hydrographs and removes the lag difference that exists between the open-
565 loop and observations.



566

567 *Figure 7 Probabilistic flood inundation maps generated by OL and EnKF techniques to simulate*
 568 *the lower limb of Harvey flood hydrograph from Aug 30 to Sep 1.*

569 Finally, to quantify the performance of EnKF and OL for generating a spatial distribution of water
 570 depth over the domain, we illustrate the ROC graphs, the *AUC* values, and Fit indices in Figure 8.

571 To calculate these measures, we ignore the temporal distributions and only report the maximum
 572 inundation maps that represent the union of flooded areas over the entire period of Harvey.

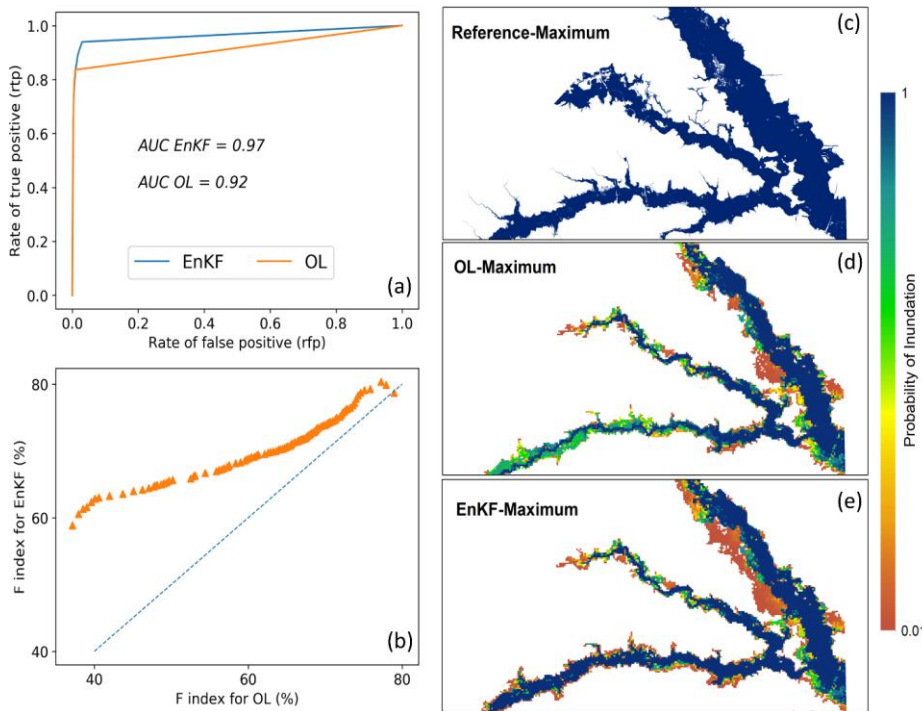
573 Comparing the EnKF and OL in Figure 8.a, the EnKF line (blue) is closer to the northwest of the
 574 *rfp-rtp* space where its *AUC* is 5% higher than the OL approach. In Figure 8.b, each point

575 represents the *F_{it}* indices for the OL and the EnKF approaches corresponding to a given threshold.
 576 Using ~~hundred number of 100~~ thresholds that ~~each ranging range~~ from [0.01,1], the probabilistic

Formatted: Font: Italic, Complex Script Font: Italic

577 maps are converted to 100 deterministic maps and the F_{\pm} indices are calculated. The position of
 578 scatters above the dash line confirms the EnKF outperforms the OL. In addition to these measures,
 579 the $[UFI, OFI]$ indices calculated for OL and EnKF approaches are [30.3, 0.26] %, and [23.4,
 580 0.4]% respectively. The low values of OFI for both approaches ($< 1\%$) show that the simulations
 581 mostly underestimate the flood inundation areas. In addition, comparing the indices of both
 582 approaches reveal that the EnKF reduces the overall underestimation by around 7%.

Formatted: Font: Italic, Complex Script Font: Italic



583

584 *Figure 8 The Receiver Operating Curves (ROC) indicating the performance of OL and EnKF*
 585 *techniques for probabilistic flood inundation mapping*

586

587

Formatted: Normal, Left, Line spacing: single

Formatted: Font: (Default) +Body (Calibri), 11 pt,
 Complex Script Font: +Body CS (Arial), 11 pt

588 5. Discussion and Conclusions

589 The main motivation in this study is to propose a DA-hydrodynamic modeling framework for real-
590 time probabilistic flood inundation mapping. Considering the coarse spatiotemporal resolution of
591 satellite data for capturing the ~~water surface elevation~~WSE, assimilating them into the
592 hydrodynamic models may not be a practical solution for an upcoming flood event. On the other
593 hand, the availability of daily discharge and ~~water surface elevation~~WSE data at gauge stations is
594 a great opportunity to establish a multivariate DA-hydrodynamic modeling framework that updates
595 the initial condition of modeling at daily scale and forecast the flood inundation areas at 1 day lead
596 time. Here, we used the EnKF data assimilation method in conjunction with a hydrodynamic
597 model to account for different sources of uncertainties involved in different layers of model
598 simulations, including the boundary conditions, model parameters, and initial condition, and
599 generate real-time probabilistic flood inundation maps. To further enhance the performance of the
600 developed framework, the discharge and water stage at two different gauges are simultaneously
601 assimilated into the LISFLOOD-FP model. The multivariate EnKF approach considers the
602 correlation between discharge at two gauges and between discharge and ~~water surface~~
603 ~~elevation~~WSE at one gauge using a modified covariance matrix and Kalman gain equation.

604 In the synthetic experiment, we examined the convergence of model parameters toward truth and
605 found that the proposed DA-hydrodynamic modeling framework can be successfully used to
606 improve the accuracy and reliability of model predictions while accounting for uncertainties
607 associated with model parameters. The channel roughness coefficient varied more rapidly than
608 the bathymetry during the temporal evolutions of these parameters showing the better
609 identifiability of this parameter. The validation results of the real experiment revealed that the
610 assimilation with the EnKF approach improves the model predictions across temporal and

611 spatial scales (i.e., discharge and water stage time series at gauges and flood maps showing the
612 maximum water depth over the simulation period). These improvements are more pronounced
613 during the falling limb of the flood hydrograph where the EnKF widens the simulated hydrograph
614 and removes the existing lag compared to the observations. Similarly, the simulated flood
615 inundation maps confirm that the OL provides discontinuous scattered maps during the flood
616 recession period while the EnKF provides a more accurate representation of the inundation areas.
617 The validation results also demonstrate that the EnKF reduces the underestimation by 7% and
618 outperformed the OL approach by around 5% for probabilistic flood inundation mapping.

619 For real-time flood inundation mapping, timely decision making is of paramount importance. The
620 time between the issuance of the warning and the occurrence of the flood is typically a short period
621 less than a day. Additionally, the flood waves propagate, inundate the affected regions and cause
622 damages rapidly. Thus, the main requirement for real-time probabilistic inundation mapping is to
623 develop a fast and efficient modeling framework that is beneficial for decision makers and
624 emergency managers. Considering the high computational expense of hydrodynamic models and
625 the need for generating a multitude of simulations in the probabilistic fashion, this study uses a
626 coarse resolution 120m DEM to maintain the efficiency of the modeling and meet the requirements
627 for practical benefits. In this study, the DA-hydrodynamic modeling framework is executed on the
628 University of Alabama High Performance Computing (UAHPC) cluster. Considering the
629 ensemble size of 100, we submit a job array with 100 cores where each core is assigned to a specific
630 member of the DA-hydrodynamic modeling simulation. The efficient hydrodynamic model setup
631 with coarse resolution DEM helps to simulate the Harvey and generate probabilistic results in 4-5
632 hours (~ 4 hours for the hydrodynamic simulation and ~20 minutes for the DA). Applying this
633 computationally efficient framework is highly beneficial, specially for the emergency response

634 agencies (e.g. FEMA), insurance companies, Water Centers, and other private companies that need
635 to forecast the inundation areas and take timely decisions a few hours before the onset of floods.

636 (Savage et al., 2016)

637 ~~To simulate flood hazards during the emergency of an upcoming flood event, using an efficient~~
638 ~~flood modeling framework is of paramount importance~~

639 ~~The coarse DEM used in this study cannot perfectly represent the watershed topography and~~
640 ~~bathymetry, and can be the main reason for the underestimation of inundation areas (F index less~~
641 ~~than 80%). Savage et al., (2016) investigated the impacts of DEM resolution on the accuracy and~~
642 ~~efficiency of probabilistic flood inundation maps generated with the LISFLOOD-FP model. They~~
643 ~~demonstrated that models with resolution less than 50 offer little gain in performance yet are more~~
644 ~~than an order of magnitude computationally expensive which can become infeasible when~~
645 ~~undertaking probabilistic analysis. They also found that the reliability of flood maps deteriorates~~
646 ~~at resolutions coarser than 100 m. Considering the medium scale of our study (> 100 km river)~~
647 ~~compared to the reach scale (~10 km river) of the work by Savage et al., (2016), here we slightly~~
648 ~~increased their suggested threshold for the DEM and demonstrated that the accuracy of results is~~
649 ~~still acceptable.~~

650 ~~However, a simplified model setup (i.e. using coarse resolution DEM; The simulation of an~~
651 ~~extreme flooding condition such as Hurricane Harvey with a simplified model setup (i.e. using a~~
652 ~~coarse DEM, assuming uniform roughness coefficient for channel and floodplain, and estimating~~
653 ~~bathymetry by lowering DEM with one parameter) for efficient flood modeling is prone to losing~~
654 ~~accuracy. Particularly, for an extreme flooding condition such as Hurricane Harvey, the simplified~~
655 ~~modeling may pose significant errors.~~ The results obtained from the simulation of the real

656 experiment demonstrated that, despite using a simplified efficient modeling setup, we can still
657 simulate the discharge, water stage, and inundation areas for an extreme flood event with [an](#)
658 acceptable accuracy while accounting for uncertainties involved in model predictions. This shows
659 that assimilating the gauge data into a simplified model setup improves the accuracy, and provides
660 an efficient probabilistic framework for real-time flood inundation mapping that considers
661 potential sources of uncertainties in different layers of modeling.

662 The time dependency that exists between the upstream and downstream gauges along a channel
663 can affect the performance of multivariate assimilation with those gauges. For future studies, using
664 a more advanced DA technique that fully characterizes the model structural uncertainty
665 (Abbaszadeh et al., 2019), and considering the time lag dependency between multiple gauges can
666 improve the performance of modeling and provide more realistic assimilation of the hydrodynamic
667 models. [Another limitation of this study is the simple assumptions made for perturbing the initial
668 condition \(water depth\), parameters \(channel roughness and river bathymetry\) and observations
669 \(WSE and discharge\). More investigation on the physically meaningful distribution of these values
670 can enhance the performance of the DA-hydrodynamic modeling framework in future studies. A
671 joint assimilation of point source gauges and remotely sensed data can also improve the reliability
672 and accuracy of the results.](#) Finally, proposing a DA-hydrodynamic modeling framework that
673 considers the DEM and channel width uncertainty can provide a more comprehensive uncertainty
674 quantification for probabilistic flood inundation mapping in future studies.

675 [An advantage of the proposed DA-hydrodynamic modeling framework is its generic format so that
676 other studies can follow the flowchart in Figure- 2 and use information in Section 3.2 and 3.3 to
677 set up the hydrodynamic model and the EnKF algorithm, respectively. To properly apply this
678 framework to other studies, first, the point source observations of WSE and discharge should be](#)

679 available at daily/sub-daily scales. In other words, the proposed framework cannot be implemented
680 in ungauged basins. Second, the modeler should have access to high performance computing
681 facilities for parallel simulation of ensemble members. Third, the hydrodynamic model should be
682 sequentially executed within the DA algorithm. The modeler should check the hydrodynamic
683 model manual and make sure that the outputs and initial conditions can be updated in a
684 sequential manner. Taking these three considerations into account, the proposed DA-
685 hydrodynamic modeling framework can be applied to any other study areas that are prone to
686 frequent flooding and provide a robust and generic tool for real-time probabilistic flood inundation
687 mapping.

Formatted: Font: (Default) Times New Roman, 12 pt,
Complex Script Font: Times New Roman, 12 pt

688 **Data availability**

689 All the data used in this study, including the gauge streamflow and water stage data and the DEMs,
690 are publicly available from the USGS website and National Elevation Dataset (NED). The
691 reference flood maps provided for Hurricane Harvey is available from the USGS report at
692 <https://pubs.usgs.gov/sir/2018/5070/sir20185070.pdf>.

693 **Author contribution**

694 KJ, PA and HM conceptualized the study and designed the synthetic and real experiments. KJ
695 developed, set up, evaluated and implemented the DA-hydrodynamic modeling framework for
696 both experiments. PA and HM provided guidance on the assimilation experiments. KJ wrote the
697 first draft of the manuscript. HM and PA provided comments and edited the manuscript.

698 **Competing interests**

699 The authors declare that they have no conflict of interest.

Acknowledgments

Partial financial support for this study was provided by the USACE contract #W912HZ2020055.

We would like to thank the anonymous reviewers for their constructive comments on the original version of the manuscript.

References

- Abbaszadeh, P., Gavahi, K., Moradkhani, H., 2020. Multivariate remotely sensed and in-situ data assimilation for enhancing community WRF-Hydro model forecasting. *Adv. Water Resour.* 145, 103721.
- Abbaszadeh, P., Moradkhani, H., Daescu, D.N., 2019. The Quest for Model Uncertainty Quantification: A Hybrid Ensemble and Variational Data Assimilation Framework. *Water Resour. Res.* 55, 2407–2431. <https://doi.org/10.1029/2018WR023629>
- Abbaszadeh, P., Moradkhani, H., Yan, H., 2018. Enhancing hydrologic data assimilation by evolutionary Particle Filter and Markov Chain Monte Carlo. *Adv. Water Resour.* 111, 192–204. <https://doi.org/10.1016/j.advwatres.2017.11.011>
- Ahmadisharaf, E., Kalyanapu, A.J., Bates, P.D., 2018. A probabilistic framework for floodplain mapping using hydrological modeling and unsteady hydraulic modeling. *Hydrol. Sci. J.* 63, 1759–1775. <https://doi.org/10.1080/02626667.2018.1525615>
- Alemohammad, S.H., McLaughlin, D.B., Entekhabi, D., 2015. Quantifying precipitation uncertainty for land data assimilation applications. *Mon. Weather Rev.* 143, 3276–3299.
- Alfieri, L., Salamon, P., Bianchi, A., Neal, J., Bates, P., Feyen, L., 2014. Advances in pan-European flood hazard mapping. *Hydrol. Process.* 28, 4067–4077. <https://doi.org/10.1002/hyp.9947>
- Anderson, J.L., Anderson, S.L., 1999. A Monte Carlo implementation of the nonlinear filtering problem to produce ensemble assimilations and forecasts. *Mon. Weather Rev.* 127, 2741–2758.
- Aronica, G., Bates, P.D., Horritt, M.S., 2002a. Assessing the uncertainty in distributed model predictions using observed binary pattern information within GLUE. *Hydrol. Process.* 16, 2001–2016. <https://doi.org/10.1002/hyp.398>
- Aronica, G., Bates, P.D., Horritt, M.S., 2002b. Assessing the uncertainty in distributed model predictions using observed binary pattern information within GLUE. *Hydrol. Process.* 16, 2001–2016. <https://doi.org/10.1002/hyp.398>
- Aronica, G.T., Franza, F., Bates, P.D., Neal, J.C., 2012. Probabilistic evaluation of flood hazard in urban areas using Monte Carlo simulation. *Hydrol. Process.* 26, 3962–3972. <https://doi.org/10.1002/hyp.8370>

Formatted: Font: 12 pt, Complex Script Font: 12 pt

736 Azimi, S., Dariane, A.B., Modanesi, S., Bauer-Marschallinger, B., Bindlish, R., Wagner, W.,
737 Massari, C., 2020. Assimilation of Sentinel 1 and SMAP-based satellite soil moisture
738 retrievals into SWAT hydrological model: The impact of satellite revisit time and product
739 spatial resolution on flood simulations in small basins. *J. Hydrol.* 581, 124367.

740 Bales, J.D., Wagner, C.R., 2009. Sources of uncertainty in flood inundation maps. *J. Flood Risk*
741 *Manag.* 2, 139–147. <https://doi.org/10.1111/j.1753-318X.2009.01029.x>

742 Bates, P.D., De Roo, A.P.J., 2000. A simple raster-based model for flood inundation simulation.
743 *J. Hydrol.* 236, 54–77. [https://doi.org/10.1016/S0022-1694\(00\)00278-X](https://doi.org/10.1016/S0022-1694(00)00278-X)

744 Brêda, J.P.L.F., Paiva, R.C.D., Bravo, J.M., Passaia, O.A., Moreira, D.M., 2019. Assimilation of
745 Satellite Altimetry Data for Effective River Bathymetry. *Water Resour. Res.* 55, 7441–
746 7463. <https://doi.org/10.1029/2018WR024010>

747 Clark, M.P., Hay, L.E., 2004. Use of Medium-Range Numerical Weather Prediction Model
748 Output to Produce Forecasts of Streamflow. *J. Hydrometeorol.* 5, 15–32.
749 [https://doi.org/10.1175/1525-7541\(2004\)005<0015:UOMNWP>2.0.CO;2](https://doi.org/10.1175/1525-7541(2004)005<0015:UOMNWP>2.0.CO;2)

750 Courtier, P., Derber, J., Errico, R.O.N., Louis, J.-F., Vukićević, T., 1993. Important literature
751 on the use of adjoint, variational methods and the Kalman filter in meteorology. *Tellus*
752 *Dyn. Meteorol. Oceanogr.* 45, 342–357.

753 Cuo, L., Pagano, T.C., Wang, Q.J., 2011. A Review of Quantitative Precipitation Forecasts and
754 Their Use in Short- to Medium-Range Streamflow Forecasting. *J. Hydrometeorol.* 12,
755 713–728. <https://doi.org/10.1175/2011JHM1347.1>

756 DeChant, C.M., Moradkhani, H., 2014. Toward a reliable prediction of seasonal forecast
757 uncertainty: Addressing model and initial condition uncertainty with ensemble data
758 assimilation and sequential Bayesian combination. *J. Hydrol.* 519, 2967–2977.

759 Di Baldassarre, G., Montanari, A., 2009. Uncertainty in river discharge observations: a
760 quantitative analysis. *Hydrol. Earth Syst. Sci.* 13, 913–921. [https://doi.org/10.5194/hess-](https://doi.org/10.5194/hess-13-913-2009)
761 [13-913-2009](https://doi.org/10.5194/hess-13-913-2009)

762 Di Baldassarre, G., Schumann, G., Bates, P.D., 2009. A technique for the calibration of hydraulic
763 models using uncertain satellite observations of flood extent. *J. Hydrol.* 367, 276–282.
764 <https://doi.org/10.1016/j.jhydrol.2009.01.020>

765 Domeneghetti, A., Vorogushyn, S., Castellarin, A., Merz, B., Brath, A., 2013. Probabilistic flood
766 hazard mapping: effects of uncertain boundary conditions. *Hydrol. Earth Syst. Sci.* 17,
767 3127–3140.

768 Durand, M., Andreadis, K.M., Alsdorf, D.E., Lettenmaier, D.P., Moller, D., Wilson, M., 2008.
769 Estimation of bathymetric depth and slope from data assimilation of swath altimetry into
770 a hydrodynamic model. *Geophys. Res. Lett.* 35.

771 Fawcett, T., 2006. An introduction to ROC analysis. *Pattern Recognit. Lett., ROC Analysis in*
772 *Pattern Recognition* 27, 861–874. <https://doi.org/10.1016/j.patrec.2005.10.010>

773 Gavahi, K., Abbaszadeh, P., Moradkhani, H., Zhan, X., Hain, C., 2020. Multivariate
774 Assimilation of Remotely Sensed Soil Moisture and Evapotranspiration for Drought
775 Monitoring. *J. Hydrometeorol.* 21, 2293–2308. <https://doi.org/10.1175/JHM-D-20-0057.1>

776 Giustarini, L., Matgen, P., Hostache, R., Montanari, M., Plaza Guingla, D.A., Pauwels, V., De
777 Lannoy, G., De Keyser, R., Pfister, L., Hoffmann, L., 2011. Assimilating SAR-derived
778 water level data into a hydraulic model: a case study. *Hydrol. Earth Syst. Sci.* 15, 2349–
779 2365.

780 Habets, F., LeMoigne, P., Noilhan, J., 2004. On the utility of operational precipitation forecasts
781 to served as input for streamflow forecasting. *J. Hydrol.* 293, 270–288.
782 <https://doi.org/10.1016/j.jhydrol.2004.02.004>

783 Hall, J.W., Tarantola, S., Bates, P.D., Horritt, M.S., 2005. Distributed Sensitivity Analysis of
784 Flood Inundation Model Calibration. *J. Hydraul. Eng.* 131, 117–126.
785 [https://doi.org/10.1061/\(ASCE\)0733-9429\(2005\)131:2\(117\)](https://doi.org/10.1061/(ASCE)0733-9429(2005)131:2(117))

786 Horritt, M.S., 2006. A methodology for the validation of uncertain flood inundation models. *J.*
787 *Hydrol.* 326, 153–165. <https://doi.org/10.1016/j.jhydrol.2005.10.027>

788 Horritt, M.S., Bates, P.D., 2002. Evaluation of 1D and 2D numerical models for predicting river
789 flood inundation. *J. Hydrol.* 268, 87–99. [https://doi.org/10.1016/S0022-1694\(02\)00121-X](https://doi.org/10.1016/S0022-1694(02)00121-X)

790 Hostache, R., Chini, M., Giustarini, L., Neal, J., Kavetski, D., Wood, M., Corato, G., Pelich, R.-
791 M., Matgen, P., 2018. Near-Real-Time Assimilation of SAR-Derived Flood Maps for
792 Improving Flood Forecasts. *Water Resour. Res.* 54, 5516–5535.
793 <https://doi.org/10.1029/2017WR022205>

794 Hostache, R., Lai, X., Monnier, J., Puech, C., 2010. Assimilation of spatially distributed water
795 levels into a shallow-water flood model. Part II: Use of a remote sensing image of Mosel
796 River. *J. Hydrol.* 390, 257–268. <https://doi.org/10.1016/j.jhydrol.2010.07.003>

797 Jafarzadegan, K., Merwade, V., 2017. A DEM-based approach for large-scale floodplain
798 mapping in ungauged watersheds. *J. Hydrol.* 550, 650–662.
799 <https://doi.org/10.1016/j.jhydrol.2017.04.053>

800 Jafarzadegan, K., Merwade, V., Saksena, S., 2018. A geomorphic approach to 100-year
801 floodplain mapping for the Conterminous United States. *J. Hydrol.* 561, 43–58.
802 <https://doi.org/10.1016/j.jhydrol.2018.03.061>

803 Kumar, S.V., Dong, J., Peters-Lidard, C.D., Mocko, D., Gómez, B., 2017. Role of forcing
804 uncertainty and background model error characterization in snow data assimilation.
805 *Hydrol. Earth Syst. Sci.* 21, 2637–2647.

806 Leach, J.M., Kornelsen, K.C., Coulibaly, P., 2018. Assimilation of near-real time data products
807 into models of an urban basin. *J. Hydrol.* 563, 51–64.

808 Lee, H., Seo, D.-J., Koren, V., 2011. Assimilation of streamflow and in situ soil moisture data
809 into operational distributed hydrologic models: Effects of uncertainties in the data and
810 initial model soil moisture states. *Adv. Water Resour.* 34, 1597–1615.

811 Lievens, H., Reichle, R.H., Liu, Q., De Lannoy, G.J., Dunbar, R.S., Kim, S.B., Das, N.N., Cosh,
812 M., Walker, J.P., Wagner, W., 2017. Joint Sentinel-1 and SMAP data assimilation to
813 improve soil moisture estimates. *Geophys. Res. Lett.* 44, 6145–6153.

814 Maidment, D.R., 2017. Conceptual Framework for the National Flood Interoperability
815 Experiment. *JAWRA J. Am. Water Resour. Assoc.* 53, 245–257.
816 <https://doi.org/10.1111/1752-1688.12474>

817 Matgen, P., Montanari, M., Hostache, R., Pfister, L., Hoffmann, L., Plaza, D., Pauwels, V.R.N.,
818 De Lannoy, G., De Keyser, R., Savenije, H.H.G., 2010a. Towards the sequential
819 assimilation of SAR-derived water stages into hydraulic models using the Particle Filter:
820 proof of concept. *Hydrol. Earth Syst. Sci.* 14, 1773–1785.

821 Matgen, P., Montanari, M., Hostache, R., Pfister, L., Hoffmann, L., Plaza, D., Pauwels, V.R.N.,
822 De Lannoy, G., De Keyser, R., Savenije, H.H.G., 2010b. Towards the sequential
823 assimilation of SAR-derived water stages into hydraulic models using the Particle Filter:
824 proof of concept. *Hydrol. Earth Syst. Sci.* 14, 1773–1785.

825 Merwade, V., Cook, A., Coonrod, J., 2008. GIS techniques for creating river terrain models for
826 hydrodynamic modeling and flood inundation mapping. *Environ. Model. Softw.* 23,
827 1300–1311. <https://doi.org/10.1016/j.envsoft.2008.03.005>

828 Moradkhani, H., Hsu, K.-L., Gupta, H., Sorooshian, S., 2005a. Uncertainty assessment of
829 hydrologic model states and parameters: Sequential data assimilation using the particle
830 filter. *Water Resour. Res.* 41.

831 Moradkhani, H., Nearing, G.S., Abbaszadeh, P., Pathiraja, S., 2019. Fundamentals of data
832 assimilation and theoretical advances. *Handb. Hydrometeorol. Ensemble Forecast.*
833 Springer Berl. Heidelb. Berl. Heidelb. 675–699.

834 Moradkhani, H., Sorooshian, S., Gupta, H.V., Houser, P.R., 2005b. Dual state–parameter
835 estimation of hydrological models using ensemble Kalman filter. *Adv. Water Resour.* 28,
836 135–147. <https://doi.org/10.1016/j.advwatres.2004.09.002>

837 Munier, S., Polebistki, A., Brown, C., Belaud, G., Lettenmaier, D.P., 2015. SWOT data
838 assimilation for operational reservoir management on the upper Niger River Basin. *Water*
839 *Resour. Res.* 51, 554–575. <https://doi.org/10.1002/2014WR016157>

840 Neal, J., Keef, C., Bates, P., Beven, K., Leedal, D., 2013. Probabilistic flood risk mapping
841 including spatial dependence. *Hydrol. Process.* 27, 1349–1363.
842 <https://doi.org/10.1002/hyp.9572>

843 Neal, J., Schumann, G., Bates, P., 2012. A subgrid channel model for simulating river hydraulics
844 and floodplain inundation over large and data sparse areas. *Water Resour. Res.* 48.
845 <https://doi.org/10.1029/2012WR012514>

846 Neal, J., Schumann, G., Bates, P., Buytaert, W., Matgen, P., Pappenberger, F., 2009. A data
847 assimilation approach to discharge estimation from space. *Hydrol. Process.* 23, 3641–
848 3649. <https://doi.org/10.1002/hyp.7518>

849 Papaioannou, G., Vasiliades, L., Loukas, A., Aronica, G.T., 2017. Probabilistic flood inundation
850 mapping at ungauged streams due to roughness coefficient uncertainty in hydraulic
851 modelling. *Adv. Geosci.* 44, 23–34.

852 Pappenberger, F., Beven, K.J., Ratto, M., Matgen, P., 2008. Multi-method global sensitivity
853 analysis of flood inundation models. *Adv. Water Resour.* 31, 1–14.
854 <https://doi.org/10.1016/j.advwatres.2007.04.009>

855 Pathiraja, S., Moradkhani, H., Marshall, L., Sharma, A., Geenens, G., 2018. Data-driven model
856 uncertainty estimation in hydrologic data assimilation. *Water Resour. Res.* 54, 1252–
857 1280.

858 Pauwels, V.R., Hoeben, R., Verhoest, N.E., De Troch, F.P., 2001. The importance of the spatial
859 patterns of remotely sensed soil moisture in the improvement of discharge predictions for
860 small-scale basins through data assimilation. *J. Hydrol.* 251, 88–102.

861 Pedinotti, V., Boone, A., Ricci, S., Biancamaria, S., Mognard, N., 2014. Assimilation of satellite
862 data to optimize large-scale hydrological model parameters: a case study for the SWOT
863 mission. *Hydrol. Earth Syst. Sci.* 18, 4485–4507. [https://doi.org/10.5194/hess-18-4485-](https://doi.org/10.5194/hess-18-4485-2014)
864 2014

865 Pedrozo-Acuña, A., Rodríguez-Rincón, J.P., Arganis-Juárez, M., Domínguez-Mora, R.,
866 Villareal, F.J.G., 2015. Estimation of probabilistic flood inundation maps for an extreme
867 event: Pánuco River, México. *J. Flood Risk Manag.* 8, 177–192.
868 <https://doi.org/10.1111/jfr3.12067>

869 Pelletier, P.M., 1988. Uncertainties in the single determination of river discharge: a literature
870 review. *Can. J. Civ. Eng.* 15, 834–850. <https://doi.org/10.1139/188-109>

871 Pinter, N., Santos, N., Hui, R., 2017. Preliminary analysis of Hurricane Harvey flooding in
872 Harris County, Texas. Retrieved UC Davis Cent. Watershed Sci.-Calif. WaterBlog
873 [Https://californiawaterblog.com/2017/09/01/preliminary-anal.-hurricane-harvey-flooding--](https://californiawaterblog.com/2017/09/01/preliminary-anal.-hurricane-harvey-flooding-harris-cty-tex/)
874 [Harris-Cty.-Tex.](https://californiawaterblog.com/2017/09/01/preliminary-anal.-hurricane-harvey-flooding-harris-cty-tex/)

875 Purvis, M.J., Bates, P.D., Hayes, C.M., 2008. A probabilistic methodology to estimate future
876 coastal flood risk due to sea level rise. *Coast. Eng.* 55, 1062–1073.
877 <https://doi.org/10.1016/j.coastaleng.2008.04.008>

878 Reichle, R.H., McLaughlin, D.B., Entekhabi, D., 2002. Hydrologic data assimilation with the
879 ensemble Kalman filter. *Mon. Weather Rev.* 130, 103–114.

880 Renard, B., Kavetski, D., Kuczera, G., Thyer, M., Franks, S.W., 2010a. Understanding predictive
881 uncertainty in hydrologic modeling: The challenge of identifying input and structural
882 errors. *Water Resour. Res.* 46. <https://doi.org/10.1029/2009WR008328>

883 Renard, B., Kavetski, D., Kuczera, G., Thyer, M., Franks, S.W., 2010b. Understanding
884 predictive uncertainty in hydrologic modeling: The challenge of identifying input and
885 structural errors. *Water Resour. Res.* 46. <https://doi.org/10.1029/2009WR008328>

886 Romanowicz, R., Beven, K., 2003. Estimation of flood inundation probabilities as conditioned
887 on event inundation maps. *Water Resour. Res.* 39.
888 <https://doi.org/10.1029/2001WR001056>

889 Sangwan, N., Merwade, V., 2015. A Faster and Economical Approach to Floodplain Mapping
890 Using Soil Information. *JAWRA J. Am. Water Resour. Assoc.* 51, 1286–1304.
891 <https://doi.org/10.1111/1752-1688.12306>

892 Savage, J.T.S., Bates, P., Freer, J., Neal, J., Aronica, G., 2016. When does spatial resolution
893 become spurious in probabilistic flood inundation predictions? *Hydrol. Process.* 30,
894 2014–2032. <https://doi.org/10.1002/hyp.10749>

895 Sheffield, J., Pan, M., Wood, E.F., Mitchell, K.E., Houser, P.R., Schaake, J.C., Robock, A.,
896 Lohmann, D., Cosgrove, B., Duan, Q., Luo, L., Higgins, R.W., Pinker, R.T., Tarpley,
897 J.D., Ramsay, B.H., 2003. Snow process modeling in the North American Land Data
898 Assimilation System (NLDAS): 1. Evaluation of model-simulated snow cover extent. *J.*
899 *Geophys. Res. Atmospheres* 108. <https://doi.org/10.1029/2002JD003274>

900 Slater, A.G., Clark, M.P., 2006. Snow data assimilation via an ensemble Kalman filter. *J.*
901 *Hydrometeorol.* 7, 478–493.

902 Tayefi, V., Lane, S.N., Hardy, R.J., Yu, D., 2007. A comparison of one- and two-dimensional
903 approaches to modelling flood inundation over complex upland floodplains. *Hydrol.*
904 *Process.* 21, 3190–3202. <https://doi.org/10.1002/hyp.6523>

905 Teng, J., Jakeman, A.J., Vaze, J., Croke, B.F.W., Dutta, D., Kim, S., 2017. Flood inundation
906 modelling: A review of methods, recent advances and uncertainty analysis. *Environ.*
907 *Model. Softw.* 90, 201–216. <https://doi.org/10.1016/j.envsoft.2017.01.006>

908 ~~Vrugt, J.A., Gupta, H.V., Nualláin, B., Bouten, W., 2006. Real time data assimilation for
909 operational ensemble streamflow forecasting. *J. Hydrometeorol.* 7, 548–565.~~

910 Xu, L., Abbaszadeh, P., Moradkhani, H., Chen, N., Zhang, X., 2020. Continental drought
911 monitoring using satellite soil moisture, data assimilation and an integrated drought
912 index. *Remote Sens. Environ.* 250, 112028. <https://doi.org/10.1016/j.rse.2020.112028>

913 [Xu, X., Zhang, X., Fang, H., Lai, R., Zhang, Y., Huang, L., Liu, X., 2017. A real-time
914 probabilistic channel flood-forecasting model based on the Bayesian particle filter
915 approach. *Environ. Model. Softw.* 88, 151–167.
916 <https://doi.org/10.1016/j.envsoft.2016.11.010>](https://doi.org/10.1016/j.envsoft.2016.11.010)

917
918 Yoon, Y., Durand, M., Merry, C.J., Clark, E.A., Andreadis, K.M., Alsdorf, D.E., 2012a.
919 Estimating river bathymetry from data assimilation of synthetic SWOT measurements. *J.*
920 *Hydrol.* 464, 363–375.
921 Yoon, Y., Durand, M., Merry, C.J., Clark, E.A., Andreadis, K.M., Alsdorf, D.E., 2012b.
922 Estimating river bathymetry from data assimilation of synthetic SWOT measurements. *J.*
923 *Hydrol.* 464, 363–375.
924 Zhang, Q., Shi, L., Holzman, M., Ye, M., Wang, Y., Carmona, F., Zha, Y., 2019. A dynamic
925 data-driven method for dealing with model structural error in soil moisture data
926 assimilation. *Adv. Water Resour.* 132, 103407.
927
928
929

Formatted: Normal, Indent: Before: 0", Hanging: 0.5"